J Mater Sci (2011) 46:2350–2358
DOI 10.1007/s10853-010-5081-4

Mechanochemical synthesis and characterization of $x\mathrm{In_2O_3}\cdot(1-x)\alpha\text{-}\mathrm{Fe_2O_3}$ nanostructure system

Monica Sorescu · Tianhong Xu · Lucian Diamandescu

Received: 2 September 2010 / Accepted: 12 November 2010 / Published online: 24 November 2010

Abstract Indium oxide-doped hematite $x\mathrm{In_2O_3}\cdot(1-x)\alpha\text{-}\mathrm{Fe_2O_3}$ ($x = 0.1$–0.7) nanostructure system was synthesized using mechanochemical activation by ball milling and characterized by XRD, simultaneous DSC–TGA, and UV/Vis/NIR. The microstructure and thermal behavior of as obtained system were dependent on the starting $\mathrm{In_2O_3}$ molar concentration x and ball milling time. XRD patterns yielded the dependence of lattice parameters and grain size as a function of ball milling time. After 12 h of ball milling, the completion of $\mathrm{In^{3+}}$ substitution of $\mathrm{Fe^{3+}}$ in hematite lattice occurs for $x = 0.1$, indicating that the solid solubility of $\mathrm{In_2O_3}$ in hematite lattice is extended. For $x = 0.3$, 0.5, and 0.7, the substitutions between $\mathrm{In^{3+}}$ and $\mathrm{Fe^{3+}}$ into hematite and $\mathrm{In_2O_3}$ lattice occur simultaneously. The lattice parameters a and c of hematite and lattice parameter a of indium oxide vary as a function of ball milling time. The changes of these parameters are due to ion substitutions between $\mathrm{In^{3+}}$ and $\mathrm{Fe^{3+}}$ and the decrease in the grain sizes. Ball milling has a strong effect on the thermal behavior and band gap energy of the as-obtained system. The hematite decomposition is enhanced due to the smaller hematite grain size. The crystallization of hematite and $\mathrm{In_2O_3}$ was suppressed, with drops of enthalpy values due to the stronger solid–solid interactions after ball milling, which caused gradual $\mathrm{In^{3+}}$–$\mathrm{Fe^{3+}}$ substitution in hematite/$\mathrm{In_2O_3}$ lattices. The band gap for hematite shifts to higher energy value, while that of indium oxide shifts to lower energy value after ball milling.

M. Sorescu (✉) · T. Xu
Department of Physics, Duquesne University, 211 Bayer Center, Pittsburgh, PA 15282-0321, USA
e-mail: sorescu@duq.edu

L. Diamandescu
National Institute of Materials Physics, P.O. Box MG-7, 077125 Bucharest, Romania

Introduction

Hematite is one of the most used oxides, with various applications in scientific and industrial fields. It can be used as semiconductor compound [1], magnetic material [2], catalyst [3], and gas sensor [4]. Indium oxide is an n-type semiconductor (band gap 3.5–3.7 eV) and is of great interest for device applications and fundamental research. Due to the good electrical conductivity and high transparency in the visible region, $\mathrm{In_2O_3}$ thin films found many technological applications in electronic devices, such as photovoltaic devices, liquid crystal displays, and solar cells [5–7]. On the other hand, $\mathrm{In_2O_3}$ thin films and powders were also widely used as gas-sensing devices, such as detection of low concentrations of oxidizing gases, $\mathrm{NO_2}$, and $\mathrm{O_3}$. However, the gas sensitivity depends strongly on the crystal structure, shape, and grain size of $\mathrm{In_2O_3}$.

There are some references concerning $\mathrm{Fe_2O_3}$–$\mathrm{In_2O_3}$-based materials. It has been reported that the sputtering of a $\mathrm{Fe_2O_3}$ layer over an $\mathrm{In_2O_3}$ thin film increases its sensitivity to $\mathrm{O_3}$ and reduces the optimal operating temperature [8]. The gas sensing behavior of $\mathrm{Fe_2O_3}$–$\mathrm{In_2O_3}$ is determined by the phase composition of the mixed oxides, their dispersion, and the $\mathrm{Fe_2O_3}$ molar concentration. It was also reported that $\mathrm{In_2O_3}$ can be used as an additive to $\mathrm{Fe_2O_3}$-based Fischer–Tropsch catalysts. The $\mathrm{In_2O_3}$–$\mathrm{Fe_2O_3}$/HZSM-5 catalyst prepared by impregnation methods was very active for the selective catalytic reduction of NO by $\mathrm{CH_4}$ [9]. Ordinarily, mixed $\mathrm{Fe_2O_3}$–$\mathrm{In_2O_3}$ materials have been prepared by conventional methods, including sol–gel procedure [10, 11], hydrothermal method under critical

conditions [12], microwave radiation method [13], and solution combustion method [14].

Due to the promoting effect of Fe_2O_3 to In_2O_3 gas sensing properties and In_2O_3 to Fe_2O_3 catalytic properties, it is of great interest to prepare the Fe_2O_3–In_2O_3 mixed oxide with different molar ratios, unique phase information and microstructures. However, complicated processes are involved in the wet chemistry methods, where accurate pH values and temperature adjustment are necessary. Especially the chemical reagents used in the wet chemistry methods are usually expensive. Therefore, this opens the possibility of applying new processing routes, searching for mixed oxides Fe_2O_3–In_2O_3 with new and optimized gas sensing and catalytic properties.

Recently, hematite [15, 16] and other metal oxides [17, 18] have increasingly been investigated for their potential in photocatalytic fuel production due to their ability to convert UV light to fuels. The main hurdle in photocatalytic fuel production is the efficient conversion of sunlight which primarily contains photons at visible wavelengths. The conversion efficiency of metal oxides is highly dependent on photon absorption, which in turn is determined by the band gap of the materials. The band gap will determine the amount of sunlight which the materials can absorb and the maximum possible solar conversion efficiency. The materials can absorb all photons in the solar spectrum with energies great or equal to the band gap. For photocatalytic production, the best band gap is approximately 2.0 eV, which can absorb significant amount of sunlight. Hematite (2.2 eV) and CuO (1.7 eV) do have band gap values in this range, however, these compounds have relatively low incident to current conversion efficiencies or experience photocorrosion. Therefore, in order to meet the widespread solar fuel production, it is necessary to develop new materials that have a band gap to maximize the photocatalytic production, but with a low cost and simple methodology.

High energy ball milling is a well-established method for preparing extended solid solutions, composite and nanostructure systems using commercially obtained oxides as starting materials. This preparation method is promising for use at a production scale due to its relatively low cost and simple operation [19]. It was found that the mechanochemical treatment of α-Fe_2O_3 and V_2O_5 for 15 h can lead to a drastic decrease of the temperature of synthesis of $FeVO_4$ catalysts [20]. The nanocrystalline composite alloys containing FeO, α-Fe, and an amorphous phase were also successfully obtained by high energy ball milling of Fe–O system, and the average size of crystallites in the produced composite with hard magnetic properties was 15–20 nm [21].

Most of the recently reported works focus the attention on the magnetic properties and gas sensor application of Fe_2O_3–In_2O_3 systems [11, 22–24], but very few ones concentrate upon the detailed structures, and effect of ball milling on the thermal behavior, band gap energy of hematite and indium oxide, especially when the progressive grain size reduction is down to nanometer dimensions and the gradual ions substitution between Fe^{3+} and In^{3+} into hematite and indium oxide lattices occurs during the ball milling process, respectively.

In this context, we report the mechanochemical activation by ball milling of $x In_2O_3 \cdot (1 - x)\alpha$-$Fe_2O_3$ nanostructure system with different molar concentrations x of In_2O_3 (cubic phase). Powder X-ray diffraction and simultaneous DSC–TGA have been used to correlate the structure, phase information, and thermal behaviors in connection with In_2O_3 concentration and ball milling time. The variation of band gap energy of hematite and indium oxide after ball milling was discussed.

Experimental

The sources of indium and iron oxides were commercially purchased from Alfa Aesar: indium oxide (cubic phase, 99.99% metals basis), and hematite (α-phase, 99% metal basis). Powders of hematite and indium oxide were milled at different molar concentrations ($x = 0.1$, 0.3, 0.5, and 0.7) in a hardened steel vial with 12 stainless-steel balls (type 440; eight of 0.25 in diameter and four of 0.5 in diameter) in the SPEX 8000 mixer mill for time periods ranging from 2 to 12 h. The ball/powder mass ratio was 5:1 and all ball milling experiments were performed in a glove box under protective argon atmosphere. Prior to their introduction in the ball milling device, the powders were manually ground to obtain fine powders.

The X-ray powder diffraction patterns of samples were obtained using a Rigaku D-2013 X-ray diffractometer with CuKα radiation ($\lambda = 1.540598$ Å) and graphite monochromator. The scanning range was 15–70° (2θ) with a step size of 0.02°. The identification of crystalline phases was accomplished by comparison with JCPDS files for indium oxide and hematite phases, respectively, and was reported after Rietveld structural refinement. The grain size was estimated using the Scherrer equation and hematite peak (104) as well as indium oxide peak (222). The lattice parameters a and c were extracted from Rietveld structural refinement of the XRD patterns. The strain and instrument effects were taken into account.

Simultaneous DSC/TGA experiments were performed using a Netzsch Model STA 449F3 Jupiter instrument with a Silicon Carbide (SiC) furnace. Samples were contained in a manufacturer's alumina crucible with an alumina lid. Series of experiments were performed using 15 ± 1 mg sample size. The atmosphere consisted of flowing

protective argon gas at a rate of 50 mL/min. DSC and TGA curves were obtained by heating samples from room temperature to 800 °C with a ramp rate of 10 °C/min. Both DSC and TGA curves were corrected by subtraction of baselines which were run under identical conditions as DSC–TGA measurement with residue of samples in the crucible. The Netzsch Proteus Thermal Analysis software was used for TGA and DSC data analysis.

An optical diffuse reflectance spectrum was obtained using a Varian Cary 5000 UV/Vis/NIR spectrometer. The sample was loaded into a Harrick Praying Mantis diffuse reflectance accessory that uses elliptical mirrors. $BaSO_4$ was used as a 100% reflectance standard. Scans were performed from 2500 to 200 nm at a rate of 600 nm/min, wavelength data were converted to electron volts, and the percent reflectance data were converted to absorbance units using the Kubelka–Munk equation [25].

Results and discussion

X-ray diffraction

Figure 1 represents the XRD patterns of indium oxide-doped hematite, $x\mathrm{In_2O_3}\cdot(1-x)\alpha\text{-}\mathrm{Fe_2O_3}$ for $x = 0.1$ and 0.3, respectively, corresponding to milling times between 2 and 12 h. For $x = 0.1$ (Fig. 1a–e), the pattern shows progressive peak broadening with milling time. This peak broadening is associated with the decrease in the grain size for both hematite and indium oxide samples. It can also be seen that the peak intensity of indium oxide decreases with the increase of milling time, indicating the gradual In^{3+} substitution of Fe^{3+} in hematite lattice. Traces of indium oxide are present in the XRD patterns up to 8 h of milling. No indium oxide phase is detected after 12 h of milling, indicating the completion of In^{3+} substitution of Fe^{3+} in the hematite lattice.

Figure 1f–j represents the XRD patterns of indium oxide-doped hematite, $x\mathrm{In_2O_3}\cdot(1-x)\alpha\text{-}\mathrm{Fe_2O_3}$ for $x = 0.3$, corresponding to milling times between 2 and 12 h. Consistent with the XRD patterns of $x = 0.1$, XRD patterns of $x\mathrm{In_2O_3}\cdot(1-x)\alpha\text{-}\mathrm{Fe_2O_3}$ for $x = 0.3$ also show progressive peak broadening with milling time, indicating the gradual In^{3+} substitution of Fe^{3+} in hematite lattice at this molar concentration. Traces of indium oxide are still present in the XRD patterns up to 12 h milling. No completion of In^{3+} substitution of Fe^{3+} in hematite lattice was observed for this molar concentration, even when ball milling time was up to 12 h, indicating that $x = 0.3$ exceeds the solubility limitation of In_2O_3 in the hematite lattice.

Consistent with the XRD patterns of Fig. 1, the progressive peak broadening as a function of ball milling time can also be seen from XRD results of $x\mathrm{In_2O_3}\cdot(1-x)\alpha\text{-}\mathrm{Fe_2O_3}$ for $x = 0.5$ and 0.7, indicating the decrease of grain sizes for both indium oxide and hematite. Compared with the completion of In^{3+} substitution of Fe^{3+} in the hematite lattice for molar concentration $x = 0.1$, indium oxide is still present in the XRD patterns even up to 12 h of milling for $x = 0.5$. This means that the molar concentration $x = 0.5$ exceeds the limit for In^{3+} substitution of Fe^{3+} in the hematite lattice, which is similar to the results for molar concentration $x = 0.3$. Progressive peak broadening with milling time can still be seen from XRD patterns for $x = 0.7$, indicating the decrease in grain sizes for both indium oxide and hematite. Indium oxide and hematite phases coexist in the XRD patterns up to 12 h milling. This means that the hematite phase can exist in $x\mathrm{In_2O_3}\cdot(1-x)\alpha\text{-}\mathrm{Fe_2O_3}$ system after 12 h milling time even when there is only a small fraction of hematite in the starting oxide mixtures. This indicates that it is more difficult for Fe^{3+} to substitute In^{3+} in the indium oxide lattice than for In^{3+} to substitute Fe^{3+} in the hematite lattice.

The grain sizes and lattice parameters of hematite and indium oxide of $x\mathrm{In_2O_3}\cdot(1-x)\alpha\text{-}\mathrm{Fe_2O_3}$ ($x = 0.5$)

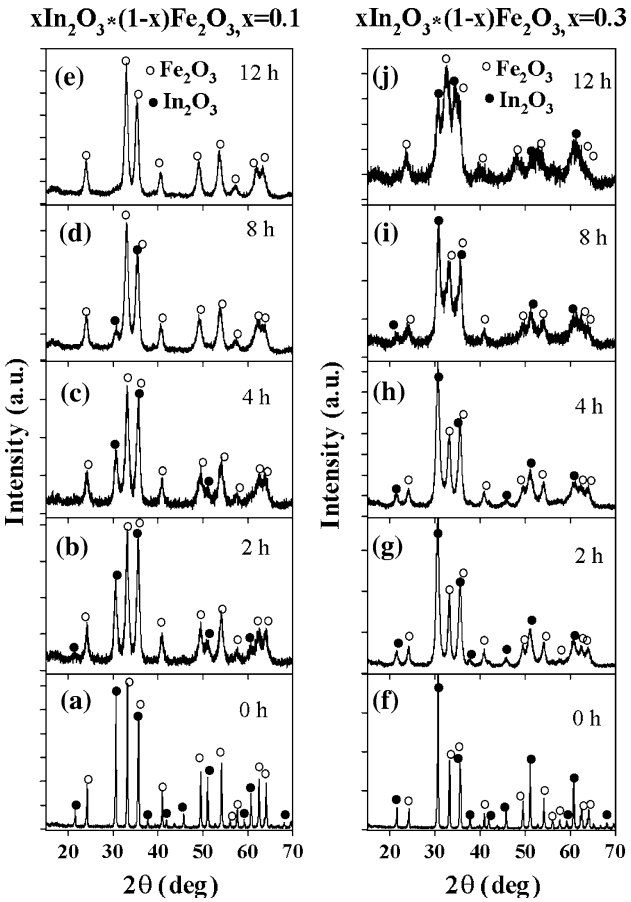

Fig. 1 XRD patterns of $x\mathrm{In_2O_3}\cdot(1-x)\alpha\text{-}\mathrm{Fe_2O_3}$ nanostructure system at $x = 0.1$ with ball milling time of **a** 0 h, **b** 2 h, **c** 4 h, **d** 8 h, **e** 12 h, and at $x = 0.3$ and ball milling time of **f** 0 h, **g** 2 h, **h** 4 h, **i** 8 h, **j** 12 h, respectively

highlighted the general trend of variations in these parameters for all other concentrations x after different durations of ball milling time (Table 1). For $x = 0.5$, the grain sizes of hematite and indium oxide decrease with the ball milling time, which is consistent with the XRD results that showed progressive peak broadening. The grain sizes of the original hematite and indium oxide powders were ~47 nm and ~41 nm, respectively. After 2 h of ball milling, the grain size of hematite and indium oxide dropped sharply to ~12 nm and ~10 nm, respectively. The grain sizes only decrease slightly at longer ball milling time, from ~7.8 nm for 4 h of milling to ~6.6 nm for 12 h of milling for hematite, and from ~10 nm to ~6.8 nm for indium oxide, indicating that the decrease in grain size mostly occurs in the first 2 h of ball milling; the increase in the ball milling time did not cause too much change in grain size after 4 h of ball milling. Similar changes in grain size of hematite and indium oxide were observed in $x\text{In}_2\text{O}_3\cdot(1-x)\alpha\text{-Fe}_2\text{O}_3$ for molar concentrations $x = 0.1$, 0.3, and 0.7 as well. The small change in the grain size at long ball milling time can be understood in terms of decreasing impact pressure on the grains. As the grain size of powder decreases, the number of grains in the zone of impact with a grinding ball increases, leading to the decrease in pressure imported to a grain and the gradual cessation of the grinding action [26]. The grains dimensions decrease down to ~7 nm at long ball milling time, evidencing the occurrence of nanoparticles in the $x\text{In}_2\text{O}_3\cdot(1-x)\alpha\text{-Fe}_2\text{O}_3$ system.

The variations in lattice parameters of hematite (a and c) and indium oxide (a only) of $x\text{In}_2\text{O}_3\cdot(1-x)\alpha\text{-Fe}_2\text{O}_3$ ($x = 0.5$) are due to the high energy ball milling which causes the decrease in grain size, the gradual In^{3+} substitution of Fe^{3+} in hematite lattice, and Fe^{3+} substitution of In^{3+} in indium oxide lattice. In particular, the decrease in the lattice parameter a of indium oxide is consistent with the radius difference between Fe^{3+} and In^{3+}, with Fe^{3+} (0.63 Å) smaller than In^{3+} (0.94 Å). The increase in both lattice parameters a and c values of hematite phases are due to the high energy ball milling effects, which decrease the grain size during the ball mill process, cause In^{3+} substitution of Fe^{3+} in hematite lattice and expand the unit cell of hematite. Similar change in lattice parameters of hematite and indium oxide were observed in $x\text{In}_2\text{O}_3\cdot(1-x)\alpha\text{-Fe}_2\text{O}_3$ for molar concentrations $x = 0.1$, 0.3, and 0.7 as well; the Rietveld refinement parameters are listed in Table 1. During the milling process, a microstrain concentrates in the lattice and increases the lattice distortion and strain energy. The increase in the lattice distortion, decrease in grain size, and ion substitutions result in the variation of lattice parameters a and c. In fact, it is well documented in literature that lattice parameter changes, either contraction or expansion, are expected when the grain sizes decrease as compared to the values of bulk materials [27].

Table 1 Rietveld refinement parameters for $x\text{In}_2\text{O}_3\cdot(1-x)\alpha\text{-Fe}_2\text{O}_3$, $x = 0.1$, 0.3, 0.5, and 0.7

Sample (x)	BMT (h)	Phase H = $\alpha\text{-Fe}_2\text{O}_3$ I = $\text{c-In}_2\text{O}_3$	Lattice parameters		Grain size (nm)
			a (Å)	c (Å)	
$x = 0.1$	0	H	5.0311	13.7386	45.9
		I	10.1161	/	40.5
	2	H	5.0349	13.7361	11.4
		I	10.0994	/	10.9
	4	H	5.0520	13.7731	8.7
		I	10.0958	/	8.4
	8	H	5.0661	13.7818	8.9
		I	10.0927	/	6.8
	12	H	5.0789	13.8046	8.9
$x = 0.3$	0	H	5.0297	13.7353	44.8
		I	10.1103	/	39.0
	2	H	5.0346	13.7418	13.1
		I	10.1055	/	10.8
	4	H	5.0446	13.7433	8.0
		I	10.0939	/	8.7
	8	H	5.0673	13.7641	7.6
		I	10.0895	/	7.2
	12	H	5.0779	13.8210	7.6
		I	10.0888	/	7.1
$x = 0.5$	0	H	5.0300	13.7342	46.9
		I	10.1176	/	40.7
	2	H	5.03478	13.7458	12.4
		I	10.1104	/	10.0
	4	H	5.03810	13.7561	7.8
		I	10.1134	/	9.6
	8	H	5.04286	13.7668	6.8
		I	10.0926	/	7.3
	12	H	5.04487	13.7744	6.6
		I	10.0925	/	6.8
$x = 0.7$	0	H	5.03310	13.7286	47.0
		I	10.1106	/	42.6
	2	H	5.0368	13.7437	13.1
		I	10.1062	/	10.7
	4	H	5.0326	13.7516	11.1
		I	10.1043	/	9.5
	8	H	5.0389	13.7730	8.2
		I	10.0932	/	8.5
	12	H	5.0422	13.7810	8.0
		I	10.0900	/	7.5
Error			±0.002	±0.002	±1

Thermal analysis by DSC–TGA

Simultaneous DSC–TGA experiments have been used to study the solid–solid interaction of mixed TiO_2–Fe_2O_3 oxide systems [28]. Differential thermal analysis (DTA) was also employed to study the thermal behavior of $Fe_2O_3 + 3Al + Fe$ powder mixture under different ball milling times [29]. It was found that the ball milling process had a great effect on the thermal behavior of the mixed oxide systems and nanocomposite powder.

The DSC–TGA curves of the original hematite and indium oxide sample are shown in Fig. 2. One exothermic peak can be been seen for the original indium oxide sample (Fig. 2b). The exothermic peak is at 489 °C, and the enthalpy value associated with this exothermic process is 2.4 kJ/g. The TGA curve of the indium oxide sample shows that there is no weight loss corresponding to the exothermic peak, and XRD results showed no phase transformation occurs when indium oxide is heated to 800 °C under Ar atmosphere. Therefore, this exothermic peak is not related to changes in the chemical formula or phase transformations. The possible explanation of this exothermic peak is that it is due to the crystallization of fine grains of indium oxide.

The detailed explanation of DSC–TGA curves of original hematite samples has been given in reference [28], with the first exothermic peak and weight loss corresponding to the decomposition of hematite under argon atmosphere (Fig. 2a).

The small amount of weight loss up to temperatures of about 120 °C for all the samples can be attributed to the surface physically adsorbed water.

Figure 3 shows the DSC and TGA curves of $x In_2O_3 \cdot (1 - x)\alpha$-$Fe_2O_3$ nanostructure system ($x = 0.1$) after ball milling for 0, 2, 4, 8, and 12 h, respectively. At 0 h of milling time, the DSC curve showed one broad peak (Fig. 3a) with the peak temperature at 501 °C. The characteristics of this peak are not just the simple sum of the DSC curves of the original hematite and indium oxide samples. The integration of this peak gives an enthalpy value of 7.55 kJ/g, which is much higher than that of the original hematite and indium oxide samples. This means that the manually ground mixture of $x In_2O_3 \cdot (1 - x)$ α-Fe_2O_3 ($x = 0.1$) shows a different thermal behavior

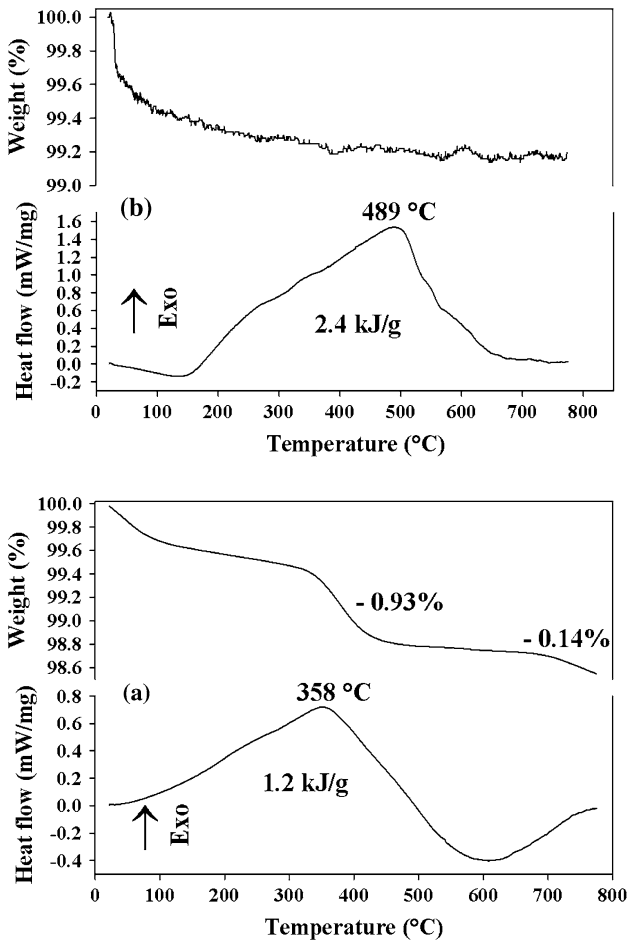

Fig. 2 DSC–TGA curves of original **a** hematite and **b** indium oxide samples

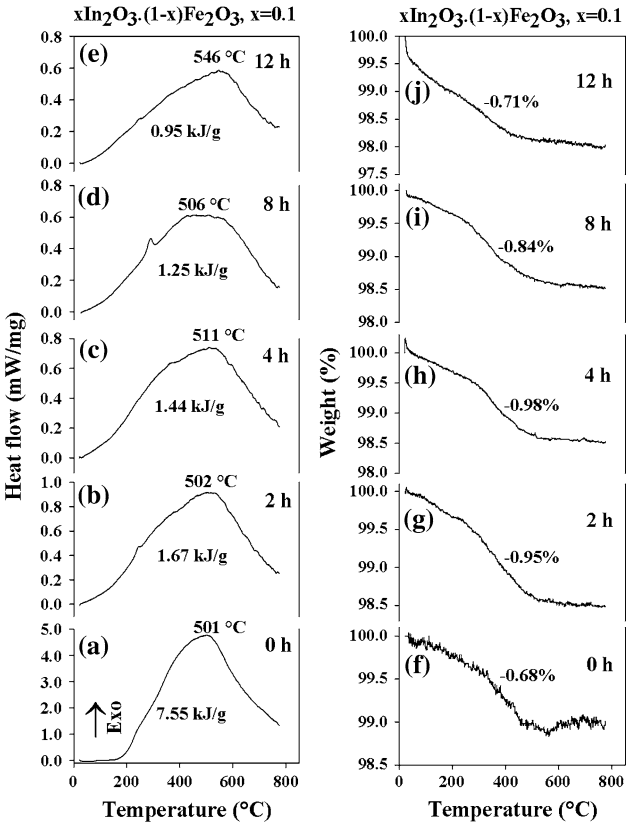

Fig. 3 DSC curves of $x In_2O_3 \cdot (1 - x)\alpha$-$Fe_2O_3$ nanostructure system ($x = 0.1$) after ball milling for: **a** 0 h; **b** 2 h; **c** 4 h; **d** 8 h; **e** 12 h, and TGA curves of $x In_2O_3 \cdot (1 - x)\alpha$-$Fe_2O_3$ nanostructure system ($x = 0.1$) after ball milling for: **f** 0 h; **g** 2 h; **h** 4 h; **i** 8 h; **j** 12 h

compared to samples with hematite or indium oxide alone. The difference in DSC curve may characterize solid–solid interactions between hematite and indium oxide and/or the phase transformation process of hematite decomposition.

Figure 3f shows the TGA curve of $x\text{In}_2\text{O}_3\cdot(1-x)$ α-Fe_2O_3 nanostructure system ($x = 0.1$) for 0 h of ball milling. A weight loss value of 0.68% can be observed for temperatures up to 600 °C, which is smaller than that of the pure original hematite (0.93%) and is reasonable considering that there is a small fraction of indium oxide in the starting materials. This means that the manual grinding process does not change the phase transition of hematite decomposition. The increase in the enthalpy for this sample must be due to the solid–solid interactions.

After ball milling for 2, 4, 8, and 12 h, the DSC curves of $x\text{In}_2\text{O}_3\cdot(1-x)\alpha$-$\text{Fe}_2\text{O}_3$ nanostructure system for $x = 0.1$ (Fig. 3b–e) change dramatically compared to the sample for 0 h of ball milling, indicating the strong effect of ball milling on the thermal behavior of $x\text{In}_2\text{O}_3\cdot(1-x)$ α-Fe_2O_3 system. The DSC curves have much smaller enthalpy values (as indicated on the graphs) and the enthalpy values of the exothermic peaks decrease with the increase of the ball milling time. The peak temperatures shifted to higher values, with the peak temperature of 501 °C for 0 h of milling time and 546 °C for 12 h of milling time. From the TGA curves of $x\text{In}_2\text{O}_3\cdot(1-x)$ α-Fe_2O_3 nanostructure system ($x = 0.1$) after different ball milling times (Fig. 3g–j), it was found that the amounts of weight loss for each sample varies with the ball milling time, indicating the solid–solid interaction between hematite and indium oxide after ball milling compared to 0 h ball-milled sample. The dramatic decrease in the enthalpy value is possibly due to the fact that the In^{3+} substitution of Fe^{3+} in the hematite lattice after ball milling suppresses the crystallization of hematite and indium oxide fine grains. The overall trend of decrease in enthalpy values as a function of ball milling time also confirms that the increase of In^{3+} substitution of Fe^{3+} in the hematite lattice (as shown by XRD) results in increased Fe_2O_3–In_2O_3 solid–solid interaction, which in turn suppresses the crystallization of fine grains.

Wongsaenmai et al. [30] studied the thermal behavior of a powder mixture of In_2O_3 and Nb_2O_5 in stoichiometric portion of InNbO_4 synthesized by solid-state reaction via vibro-milling technique. The ~4% weight loss above 650 °C was assigned to solid-state reaction occurring between In_2O_3 and Nb_2O_5, which is not the case in our experiment since the weight loss is related to the molar concentration of hematite. Moreover, the solid-state reaction between In_2O_3 and Nb_2O_5 occurred at higher temperature and had a much larger weight loss.

Table 2 summarized the peak temperature, enthalpy, and weight loss extracted from the DSC and TGA curves of $x\text{In}_2\text{O}_3\cdot(1-x)\alpha$-$\text{Fe}_2\text{O}_3$ nanostructure system after ball

Table 2 Peak temperature, enthalpy, and weight loss extracted from the DSC and TGA curves of $x\text{In}_2\text{O}_3\cdot(1-x)\alpha$-$\text{Fe}_2\text{O}_3$, $x = 0.1$, 0.3, 0.5, and 0.7

Sample (x)	BMT (h)	Peak temperature (°C)	Enthalpy (kJ/g)	Weight loss (%)
$x = 0.1$	0	501	7.55	−0.68
	2	502	1.67	−0.95
	4	511	1.44	−0.98
	8	506	1.25	−0.84
	12	546	0.95	−0.71
$x = 0.3$	0	523	2.60	−0.71
	2	362, 535	2.07	−0.83
	4	478	0.98	−0.81
	8	363, 510	0.83	−0.89
	12	548	0.74	−0.90
$x = 0.5$	0	546	3.79	−0.44
	2	348, 549	1.89	−0.57
	4	357, 517	1.93	−0.60
	8	356, 518	1.91	−0.64
	12	365	0.92	−0.65
$x = 0.7$	0	406, 559	4.07	−0.31
	2	365	0.41	−0.50
	4	360	0.42	−0.59
	8	347	0.47	−0.61
	12	339	0.46	−0.65
Error		±3	±0.05	±0.02

milling for 0, 2, 4, 8, and 12 h, respectively. For $x = 0.3$ at 0 h of milling time, the DSC curve shows one broad peak with the peak temperature at 523 °C. The integration of this peak gives an enthalpy value of 1.60 kJ/g, which is between that of the original hematite and indium oxide samples. A weight loss of 0.71% can be observed at a temperature up to 600 °C, which is smaller than that of the original hematite (0.93%). The exothermic peak extended to higher temperature (>800 °C). Change in enthalpy value (1.60 kJ/g) for this sample is due to the increase of In_2O_3 molar concentration, such that there are much more Fe_2O_3–In_2O_3 interactions upon heating. After ball milling for 2, 4, 8, and 12 h, the DSC curves of $x In_2O_3 \cdot (1 - x)\alpha$-$Fe_2O_3$ nanostructure system for $x = 0.3$ also change dramatically compared to those of 0 h ball-milled sample, indicating the strong effect of ball milling on the thermal behavior of $x In_2O_3 \cdot (1 - x)\alpha$-$Fe_2O_3$ system for $x = 0.3$. The DSC curves of ball-milled samples have a completed exothermic peak and with much smaller enthalpy values than those of 0 h ball-milled sample. From the TGA curves of $x In_2O_3 \cdot (1 - x)\alpha$-$Fe_2O_3$ ($x = 0.3$) after different ball milling times, it was found that there are slightly higher amounts of weight loss ($0.85 \pm 0.05\%$) for each sample, indicating there are slightly larger amounts of hematite that decomposes to magnetite upon heating under Ar atmosphere after ball milling. The dramatic decrease in the enthalpy values is possibly due to In^{3+} substitution of Fe^{3+} in the hematite lattice and Fe^{3+} substitution of In^{3+} in the indium oxide lattice after ball milling, which suppresses the crystallization of hematite and indium oxide fine grains. The overall trend of decrease in enthalpy value as a function of ball milling time also confirmed that the In^{3+} substitution of Fe^{3+} in the hematite lattice as shown by XRD increases the Fe_2O_3–In_2O_3 solid–solid interaction, which in turn suppresses the crystallization of fine grains.

The $x In_2O_3 \cdot (1 - x)\alpha$-$Fe_2O_3$ nanostructure system with $x = 0.5$ and 0.7 after ball milling shows similar thermal behavior as that of $x = 0.1$ and 0.3, respectively. The increase of weight loss is due to the decrease of the grain size of hematite after ball milling process. The weight loss values increase slightly with the increase of ball milling time, indicating that hematite with smaller grain sizes is easier to decompose to magnetite upon heating under Ar atmosphere after longer ball milling time.

Optical diffuse reflectance spectroscopy

The optical diffuse reflectance spectrum for samples hematite, indium oxide, and $x In_2O_3 \cdot (1 - x)\alpha$-$Fe_2O_3$ ($x = 0.5$) with different ball milling times were shown in Fig. 4.

For hematite, the valence and conduction bands arise from crystal field splitting of the Fe 3*d* levels due to the octahedral coordination of oxygen around Fe [31]. As shown in Fig. 4a, diffuse reflectance spectra of original hematite exhibited a band gap energy value of ~2.2 eV, which is consistent with reported value for bulk hematite [32, 33]. Indium (III) oxide forms bixbyite-type cubic crystals. Its band gap has recently been reported to be in the range from 2.9 to 3.7 eV [34, 35]; the measured band gap energy of the original indium oxide has a value of ~3.5 eV. For sample $x In_2O_3 \cdot (1 - x)\alpha$-$Fe_2O_3$ ($x = 0.5$) with 0 h of milling time, just after physically mixing hematite–indium oxides, the band gap energy of hematite and indium oxide changes slightly, with a value of ~2.16 eV for hematite and ~3.34 eV for indium oxide, respectively. This variations in band gap energy of hematite and indium oxide are attributed to the change in density of states of the 2*p* level for O and 3*d* level for In and Fe. A similar change in band gap energy was also observed in Fe-doped TiO_2 system [36].

After 12 h of milling time, the band gap energy of hematite increases to ~2.23 eV, which is higher than that

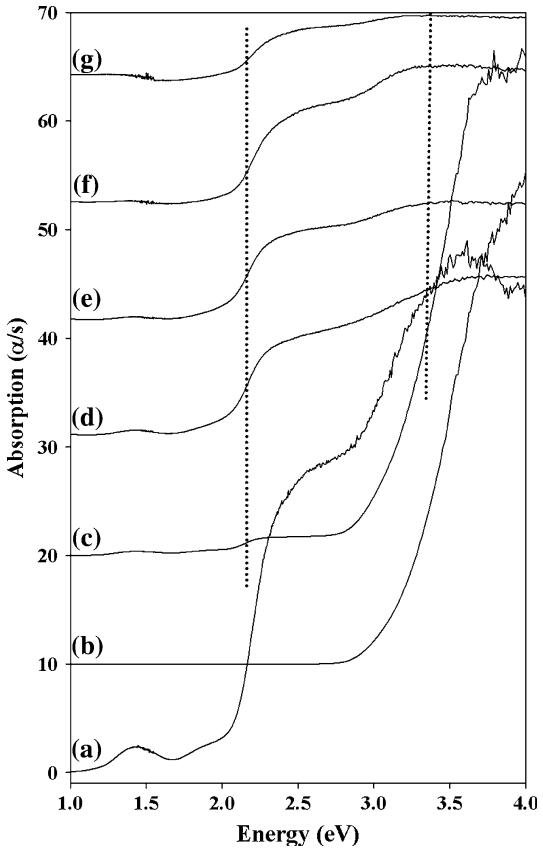

Fig. 4 Optical diffuse reflectance spectrum converted to absorption for samples: (*a*) original hematite, (*b*) original indium oxide, and samples $x In_2O_3 \cdot (1 - x)\alpha$-$Fe_2O_3$ ($x = 0.5$) after ball milling for (*c*) 0 h; (*d*) 2 h; (*e*) 4 h; (*f*) 8 h; (*g*) 12 h. The *dashed lines* are guides to the eye regarding the band gap energy shift. On the *y*-axis α is the absorbance and *s* is the scattering coefficient constant

of original hematite or 0 h ball-milled hematite–indium oxide sample. The band gap energy of indium oxide decreases to ~2.94 eV. It has been reported that the optical band gap of hematite samples that are around 30 or 8 nm in diameter are identical [37], therefore, the variation in band gap energy of hematite and indium oxide is not due to the grain size effect. The variation in grain size of hematite and indium oxide as a function of ball milling time also confirmed that (Table 1), after 2 h of ball milling, the grain size only decreases slightly, while the change of band gap energy is very pronounced, as indicated by the guide line. Therefore, the change in band gap energy of hematite and indium oxide is mainly due to the gradual ion substitution between In^{3+} and Fe^{3+} in hematite and indium oxide lattices during milling process, respectively. This means the simple, low cost ball milling method can be used to tune the band gap energy by adjusting ball milling time and molar ratio of mixed oxides, which have the importance in photocatalytic fuel production.

Conclusions

Indium oxide-doped hematite nanostructure, $x In_2O_3 \cdot (1 - x)\alpha\text{-}Fe_2O_3$ ($x = 0.1$, 0.3, 0.5 and 0.7), were synthesized by mechanochemical activation technique. The system was further characterized by XRD, simultaneous DSC–TGA, and UV/Vis/NIR. The grain size decreases with the increase of ball milling time, as demonstrated by Scherrer formula. At lower In_2O_3 molar concentrations ($x = 0.1$), the completion of In^{3+} substitution of Fe^{3+} in hematite lattice occurred at long ball milling time. Lattice parameters of hematite and indium oxide vary as a function of ball milling time due to the decrease in grain size and ions substitution between In^{3+} and Fe^{3+}. Simultaneous DSC–TGA measurements revealed that the mechanochemical activation by ball milling has a strong effect on the thermal behaviors of this nanostructure system. The enthalpy of the exothermic peak dropped even after 2 h of milling time, indicating the strong interaction between In_2O_3 and $\alpha\text{-}Fe_2O_3$, which suppresses the crystallization of both hematite and In_2O_3 grains. The change in weight loss of hematite was caused by the decrease of grain sizes and the degree of ion substitutions between Fe^{3+} and In^{3+} in the corresponding lattices. The band gap energy of hematite and indium oxide in the $x In_2O_3 \cdot (1 - x)\alpha\text{-}Fe_2O_3$ system varies as a function of ball milling time, the band gap energy of hematite increases with the increase of milling time, while that of indium oxide decreases due to the change of electron structure caused by the ions substitution between Fe^{3+} and In^{3+} under ball milling process.

Acknowledgement This work was supported by the National Science Foundation under grant DMR-0854794.

References

1. Wang GX, Gou XL, Horvat J, Park J (2008) J Phys Chem C 112:15220
2. Raffaella B, Etienne S, Cinzia G, Fabia G, Mar GH, Miguel AG, Roberto C, Pantaleo DC (2009) Phys Chem Chem Phys 11:3680
3. Krishnamoorthy S, Rivas JA, Amiridis MD (2000) J Catal 193:264
4. Sorescu M, Diamandescu L, Tomescu A, Tarabasanu-Mihaila D, Teodorescu V (2008) Mater Chem Phys 107:127
5. Gulo A, Ivanovskaya M, Pfau A, Weimar U, Göpel W (1997) Thin Solid Films 307:288
6. Perez-Maquela LA, Wang L, Matijević E (1998) Langmuir 14:4397
7. Gurlo A, Bârsan N, Ivanovskaya M, Weimar U, Göpel W (1998) Sens Actuators B 47:92
8. Takada T, Suzuki K, Nakane M (1993) Sens Actuators B 13–14:404
9. Wang XD, Zhao XQ, Shen JY, Sun XY, Zhang T, Lin LW (2002) Phys Chem Chem Phys 4:2846
10. Nomura K, Sakuma J, Ooki T, Takeda M (2008) Hyperfine Interact 184:117
11. Ivanovskaya M, Kotsikau DA, Taurino A, Siciliano P (2007) Sens Actuators B 124:133
12. Sorescu M, Diamandescu L, Tarabasanu-Mihaila D (2004) J Phys Chem Solids 65:1719
13. Takizawa H, Uheda K, Endo T (2000) J Am Ceram Soc 83:2321
14. Yu J, Duan LB, Wang YC, Rao GH (2009) J Phys Chem Solids 182:1563
15. Cesar I, Kay A, Martinez JAG, Grätzel M (2006) J Am Chem Soc 128:4582
16. Kay A, Cesar I, Grätzel M (2006) J Am Chem Soc 128:15714
17. Alexander BD, Kulesza PJ, Rukowska L, Solarska R, Augustynski J (2008) J Mater Chem 18:2298
18. Ihara T, Miyoshi M, Ando M, Sugihara S, Iriyama Y (2001) J Mater Sci 36:4201. doi:10.1023/A:1017929207882
19. Tojo T, Zhang QW, Saito F (2008) J Mater Sci 43:2962. doi:10.1007/s10853-006-1472-y
20. Klissurski D, Iordanova R, Radev D, Kassabov ST, Milanova M, Chakarova K (2007) J Mater Sci 39:5375. doi:10.1023/B:JMSC.0000039248.33392.ed
21. Yagodkin YD, Lileev AS, Grishina EN (2007) J Mater Sci 39:5255. doi:10.1023/B:JMSC.0000039222.53614.e6
22. Bérardan D, Guilmeau E (2007) J Phys Condens Matter 19: 236224 (9 pp)
23. Singhal A, Achary SN, Manjanna J, Jayakumar OD, Kadam RM, Tyagi AK (2009) J Phys Chem C 113:3600
24. Kohiki S, Murakawa Y, Hori K, Shimooka H, Tajiri T, Deguchi H, Oku M, Arai M, Mitome M, Bando Y (2005) Jpn J Appl Phys 44:L979
25. Kubelka P, Munk F (1931) Z Tech Phys 12:593 (English translated by Westin S.)
26. Nath AK, Jiten C, Singh KC (2010) Physica B 405:430
27. Sánchez LC, Arboleda JD, Saragovi C, Zysler RD, Barrero CA (2007) Physica B 389:145
28. Sorescu M, Xu TH, Diamandescu L (2010) Mater Character 61:1103
29. Khodaei M, Enayati MH, Karimzadeh F (2008) J Mater Sci 43:132. doi:10.1007/s10853-007-2123-7
30. Wongsaenmai S, Yimnirun R, Ananta S (2007) J Mater Sci 42:3754. doi:10.1007/s10853-006-0404-1

31. Morin FJ (1954) Phys Rev 93:1195
32. Marusak LA, Messier R, White WB (1980) J Phys Chem Solids 41:981
33. Dare-Edwards MP, Goodenough JB, Hamnett A, Trevellick PR (1983) J Chem Soc Faraday Trans 79:2027
34. Walsh A, Silva JLD, Wei SH, Körber C, Klein A, Piper L, DeMasi A, Smith KE, Panaccione G, Torelli P, Payne DJ, Bourlange A, Egdell RG (2008) Phys Rev Lett 100:167402
35. King PDC, Veal TD, Fuchs F, Wang CY, Payne DJ, Bourlange A, Zhang H, Bell GR, Cimalla V, Ambacher O, Egdell RG, Bechstedt F, McConville CF (2009) Phys Rev B 79:205211
36. Thimsen E, Biswas S, Lo CS, Biswas P (2009) J Phys Chem C 113:2014
37. Gilbert B, Frandsen C, Maxey ER, Sherman DM (2009) Phys Rev B 79:035108